Contents lists available at ScienceDirect

Composites Part C: Open Access

Multi-physical modelling, design optimization and manufacturing of a composite dielectric solar absorber

Nikhar Khanna [a,b], Mohamed El Hachemi [a,*], Ruben Sevilla [c], Oubay Hassan [c], Kenneth Morgan [c], Emanuele Barborini [a], Salim Belouettar [a]

[a] Luxembourg Institute of Science and Technology, 5, Avenue des Hauts Fournaux, Esch/Alzette, L-4362, Luxembourg
[b] Luxembourg University, 2, avenue de l'Université, Esch/Alzette, L-4365, Luxembourg
[c] Swansea University, Bay Campus, Fabian Way, Swansea, SA1 8EN, Wales, United Kingdom

ARTICLE INFO

ABSTRACT

The work presented involves the multiphysical modelling, simulation and design optimization of a key component of a Solar Selective Coatings (SSC). The investigated SSC absorber consists of a near homogeneous distribution of nanoparticles of Titanium Nitride (TiN) in a matrix of Aluminium Nitride (AlN), to form a composite dielectric. With the aim of achieving high absorbance in the visible region of the spectrum and minimum reflectance in the infrared region of the spectrum, our work highlights the numerical design, the synthesis and optical characterization of a composite dielectric of approximately 500 nm thickness. A bottom-up approach for the preparation of a stack with alternate layers, consisting of a distribution of TiN nanoparticles with a layer of AlN on top, was adopted. The TiN nanoparticles, laid on a substrate (Silicon/Glass) by wet chemical method, are coated with conformal layer of AlN, via Plasma-enhanced Atomic Layer Deposition (PE-ALD). The control of the morphology at the nanoscale is fundamental in improving the optical performance of the material. For this reason, two composites were prepared. One starting with TiN dispersions made with dry TiN powder and deionized water, and the other with ready-made TiN dispersions. In both composites, the particles were 20–30 nm in diameter. In both the cases, fewer clusters of about 0.5–1 μm of TiN particles were present however, enough steps were taken to minimize these clusters into smaller particles. Parameters, such as the size of TiN nanoparticles, the thickness of AlN thin film, were revealed by the numerical simulations, performed using Wave-Optics module in COMSOL Multiphysics. The work showcased clearly compares the two kinds of composites, using scanning electron microscope, X-ray photoelectron spectroscopy and electrical conductivity measurement. In addition, the optical performance of the two prepared composites is used as a means of validating the computational model.

1. Introduction

Solar-thermal energy conversion is a promising technology that enables efficient energy harvesting from concentrated solar power (CSP). Recently, a lot of interest has been directed at composite metal–insulator based absorbers, as they offer high solar selectivity, depending on the constituent materials for metal and insulator. A reliable analysis of the complex coupled physical fields are crucial to the design and fabrication of such composite structures [1–4].

CSP is a prime technology in renewable energies for solar energy conversion. Spectrally-selective solar absorbers are extensively used in harvesting of sunlight for a broad range of applications [5–9]. Spectrally-selective solar absorbers play an important role in enhancing solar-to-thermal conversion efficiency, absorbing the major part of solar

radiation energy in a broad wavelength regime, while suppressing the infrared (IR) re-radiation that is generated by heating of the solar absorber [8]. Thus, solar absorption and thermal emittance are the two main physical criteria indicating the performance of solar-to-thermal conversion devices. According to the European Strategic Energy Technology (SET) Plan, the target is to generate 27% of EU electricity by solar energy, by the year 2030. The report states that it is intended to get to 11% CSP share of the global electricity by 2050 [10].

Selective solar absorbers are being categorized into different types, in which each type of structure plays a different role in maximizing absorption and minimizing emittance for best efficiency [11–14]. The work presented here is focused on metal–dielectric composites (named cermets) [15] which is a fundamental unit of the SSC that we aim to

---

* Corresponding author.
  E-mail address: mohamed.elhachemi@list.lu (M. El Hachemi).

prepare in our future work. These absorbers consist of metal particles embedded in a dielectric matrix and get their efficacy from the synergic combination of the properties of the constituent materials. When such a composite is integrated in SSC which when coated on a highly reflecting metal surface as a thin film, the resulting coating becomes a good candidate for CSP applications. The cermet layer is reflective in the thermal IR region and strongly absorbs in the visible region of the solar spectrum, because of interband transition in the metal and the small particle resonance. The solar selectivity of these cermet absorbers can be adjusted by selecting an appropriate thickness for the coating, the concentration of the particles, their size and orientation in the dielectric matrix [15,16]. In a typical solar thermal engineering system, the sunlight incident on the absorber layer is converted into a heat flux and delivered to the thermal system, where it does the desired work of heating and cooling. The thermal radiations leak at the surface as radiative and convective thermal losses. As a result, the ideal curve of an effective solar absorber is a step function between a minimum value of reflectance (high absorptivity) in the visible (VIS) wavelength range and a high reflectance (low emissivity) in the mid-infrared thermal radiation range (IR) so as to reduce the thermal leakage by radiation. Ideally the lower reflectance should be 0% while the upper limit for the same would be 100%; however, in reality these values cannot be attained. Thus, in the present investigation we are targeting characteristics similar to the ideal solar absorber from the metal–dielectric composites, making it obvious that if a component from the entire system shows similar characteristics, we would reach a step closer in obtaining a near perfect absorber.

SSC suffer a major setback due to the materials they are made of thus, selecting the appropriate materials for the SSC is an influential step in its performance. TiN has gained much attention in the context of materials for CSP, due to its peculiar properties, particularly its high chemical and thermal stability, together with its low electrical resistivity. In addition, its high melting point (2930 °C) and high hardness of TiN also make it an ideal material to be embedded into a dielectric matrix for CSP applications [17–20]. Moreover, it has been reported that TiN is an excellent candidate for high-temperature plasmonic applications, while conventional plasmonic materials like gold and silver are not suitable because of their relatively low melting point and softness [17,19,21].

AlN is known to provide hard coatings, that are chemically and thermally stable at elevated temperatures. It has a wide band gap (6.0–6.2 eV) [22,23], so that it is transparent in the visible region, with high thermal conductivity [24] and a high melting point (2200 °C). Thus, it is suitable as a dielectric matrix for CSP applications. In air, the oxidation of AlN is known to occur at (700 °C) [25,26]. However, a passivation layer of alumina (Al_2O_3) is typically observed on the surface of AlN thin films, deposited in vacuum conditions, upon exposure to air. The deposition process itself can introduce a certain amount of oxygen into the material, leading to the presence of alumina in the core of the coatings. But, as the properties remain similar to those of AlN, i.e. low absorption of solar radiation, high electrical insulation, and high thermal conductivity, the presence of an alumina fraction into AlN does not affect the overall characteristics of the AlN dielectric matrix.

Our work involves the synthesis of a dielectric composite, a key component of the SSC, made of a distribution of TiN NPs embedded into an AlN matrix, with well-defined size and spacing of TiN NPs, supported by a numerical simulation driven design of the material. Numerical simulations show that the optical properties of the composite can be tuned by controlling the distribution of TiN particles laid inside the AlN matrix, allowing prediction of the optimal configuration.

This article is organized into the following sections: 2, wave-optics modelling of the AlN – TiN composite describes the computational studies employed to derive certain important parameters for the optimal design of the dielectric composite. Simulations were performed using multiscale approach where the effective optical properties of the composite were calculated in the nanoscale-model and placed in the

macro-model for optical performance predictions; 3, describes the stepwise details adopted during the synthesis of the dielectric composite with two different approaches; 4, this section explains the characterization results using Scanning Electron Microscope (SEM), X-ray Photoelectron Spectroscopy (XPS), electrical conductivity measurement and optical measurement are mentioned. A comparison between the two composites prepared experimentally, and the numerical model is shown, wherever necessary.

2. Modelling of the composite dielectric absorber

The modelling consists of two steps — modelling the wave optics interaction with nanoparticles and subsequently the wave propagation through the composite film in steady state. electromagnetic interactions are simulated by solving Maxwell's equations (1) for the electric field in the frequency domain [27].

$$\begin{cases} \dfrac{\partial \vec{D}}{\partial t} &= \nabla \times \vec{H} \\[2mm] \dfrac{\partial \vec{B}}{\partial t} &= -\nabla \times \vec{E} \\[2mm] \nabla \cdot \vec{B} &= 0 \\[2mm] \nabla \cdot \vec{D} &= 0 \end{cases} \tag{1}$$

The wave optics propagation solved in frequency domain and steady state respectively by Finite Element Method. For the nanostructured architecture (Fig. 1), the length scale parameters are taken from experimental measurements. The maximum mesh element size used in the electromagnetic simulations is 5 nm. This is much smaller compared to the minimum wavelength λ simulated. The wave-optics module in COMSOL Multiphysics [28] is used to predict the optimal design of the absorber coatings, starting with the interaction of light with the nanoparticles. First, we built a nanoscale model, where we specified the dimensions and volume fraction (vf) of TiN NPs into the AlN matrix. Instead of modelling an array of TiN NPs with AlN thin film over the bulk silicon, we used a single unit cell along with a Floquet periodic boundary condition on the sides [29,30]. This approach significantly reduces the computation time of the model, without compromising the accuracy of the results. The refractive indexes of AlN and TiN are dispersive over the frequency spectrum, for our simulations we used the data available from database https://refractiveindex.info. In order to ensure sufficient accuracy and mesh convergence while doing parametric sweep calculations over the spectrum 250 nm–2.5 µm, the PML is always maintained to be $\lambda/2$ and eight prismatic elements, the air space between PML and unit cell is three prismatic elements. Tetrahedral elements are used to mesh unit cell including the NP and the element size is chosen to be fine enough (5 nm) to resolve the particle curvature and also kept below $\lambda/8$. Quadratic elements are used with direct solver which counts for 54000 dof which have shown good convergence rate for all frequencies. We simulated nanostructures, varying the size of TiN NPs, their volume fraction in AlN matrix and their intricacies, aiming at enhancing the absorbance of the desired design. The performance of the proposed design will be validated experimentally by a comparison with the prediction of the numerical model. The aim of the numerical optimization is to determine the size of the NPs and their density, i.e the number of unit cells in the composite layer, so that the material maximizes the absorption in the visible fraction of the solar spectrum, as well as the reflection in the IR region of the spectrum. We performed simulations using a multiscale approach for TiN particles inside a AlN matrix. Simulations enabled us to derive the optimal values for the TiN particle diameter D and the vf of TiN NPs inside the AlN matrix. Fig. 1 shows the constructed nanoscale-model, where a single TiN NP is buried in a AlN matrix, forming a single unit cell. The perfectly matched layer (PML), indicated in yellow, is a domain/layer that is included to mimic a non-reflecting infinite domain. The top and bottom surface, between the PML and the air, is considered as the port from which the excitation of the incident wave is activated. In Fig. 2, it is clearly seen that TiN particle diameter of D = 20 nm demonstrates
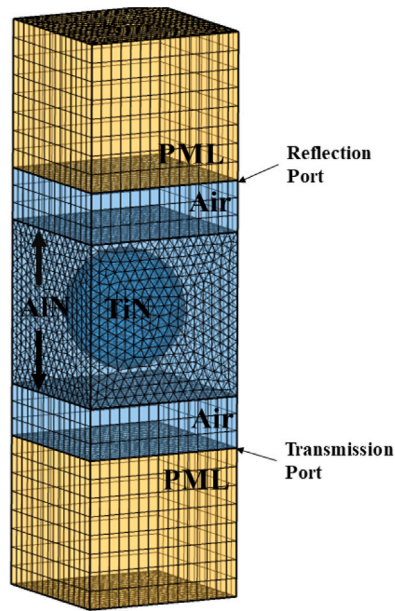
Fig. 1. Single unit cell modelled with TiN NP inclusion in AlN host. PML thickness is kept as $\lambda/2$, the air space fixed to be three elements between the PML and the unit cell. Floquet-PBC is applied to parallel sides to mimic infinite surface. the port surfaces are used to apply the incident wave and compute the scattering parameters.
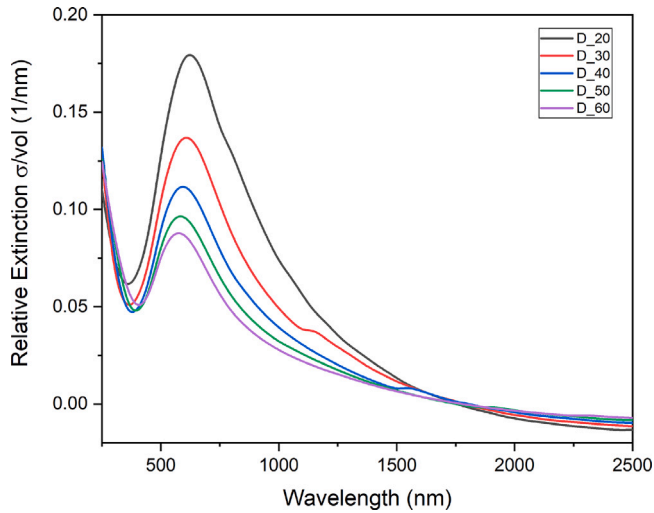

Fig. 3. The absorbance results showing that 20% volume fraction of TiN provides good absorption over the visible and high reflection in the IR region of the spectrum.

Fig. 2. Extinction cross section for various particle sizes showing that small particle diameter (D = 20 nm) gives better performance.

the best curve in terms of relative extinction of the incident wave with wavelength. We investigated, on the unit-cell, the extinction cross-section relative to the particle volume, ranging from 20 nm–60 nm TiN particle diameter. The extinction cross-section, sometimes called the attenuation cross-section, [31,32], is the area which, when multiplied with the irradiance of electromagnetic waves incident on the unit cell, gives the total radiant flux absorbed by the unit cell formed with the TiN particle buried in the AlN matrix. We define

$$\sigma_{ext} = \sigma_{sca} + \sigma_{abs} \tag{2}$$

where σ_{ext} is the measure of the dissipation of light in a medium, σ_{sca} is the amount of light scattered inside the material by particles and σ_{abs} is the amount of light absorbed, as Joule loss, in the material.

To know the vf of TiN NPs in AlN matrix for least reflectance in the visible spectrum and maximum reflectance in the infrared spectrum,
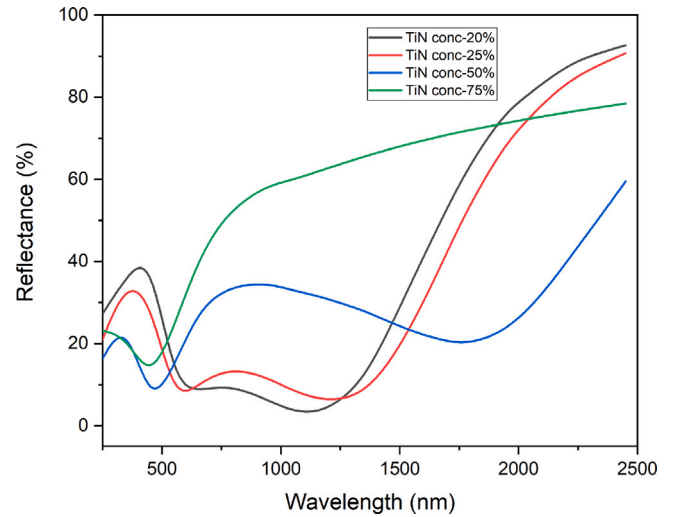
it was necessary to construct a macro-model numerically. Properties like reflectance depends on the thickness, and is obtained using a two-scale approach. This method is built upon the calculation of scattering S-parameters that are associated with complex reflection and transmission coefficients. After the S-parameters were obtained from the micro-model that was constructed above, they are used to retrieve the optical effective parameters *n* and *k* using technique described in [33,34]. These values are fed into the constructed macro-model similar to the one shown in Fig. 4 to evaluate its reflectance in the required VIS–IR spectrum. Four different volume concentrations, in the range 20%–75%, were investigated, while the diameter of TiN was fixed at 20 nm. The thickness of the composite in the macro-model was taken as 1 μm. Fig. 3 shows the computed reflectance, for different volume fraction of TiN NPs in the AlN matrix. For the composite with vf = 75% of TiN NPs inside the AlN matrix, a high reflectance in the visible and IR region is seen, which is not what we are seeking. The composite with vf = 20% of TiN gives the best absorbance (least reflectance) in the visible region and high reflectance in the IR. The 20% volume fraction has a peculiar characteristic of a sharp filter between the reflectance in the visible and the IR region of the spectrum. In all our subsequent experiments, we used 20 nm diameter TiN NPs and tried to control the concentration of TiNNPs close to 20%. Given the two parameters, the diameter, and the volume fraction of TiN NPs inside AlN matrix, for best absorption, we retrieve the effective parameters of the homogenized composite dielectric in terms of refractive index (*n*) and extinction coefficient (*k*). These parameters then help us in obtaining the reflectance of the macro-model that corresponds to the composite prepared experimentally.

The macro-model describing the complete structure of the composite was successively refined according the outcomes of the experimental work. These regarded in particular the total thickness and the presence of a certain fraction of alumina (Al_2O_3) in AlN layers (see XPS results in Section 4.2). Fig. 4 shows the computational model of the homogenized media with a thinner dielectric-1 on top of a much thicker dielectric-2. Floquet boundary conditions were applied separately to the pair of two opposite boundaries to simulate a large surface [29]. The effective parameters, *n* and *k*, retrieved from the nanoscale-model (unit cell) were placed in the homogenized dielectrics of the macro-model, for evaluating the optical performance of the selective absorber layer, in terms of absorbance and reflectance over the frequency range of the visible light which is shown in Section 4—Fig. 17. The *n* and *k* values for dielectric-1 were retrieved from a unit cell that consists of an inclusion of 35% volume fraction of alumina inside a AlN matrix.
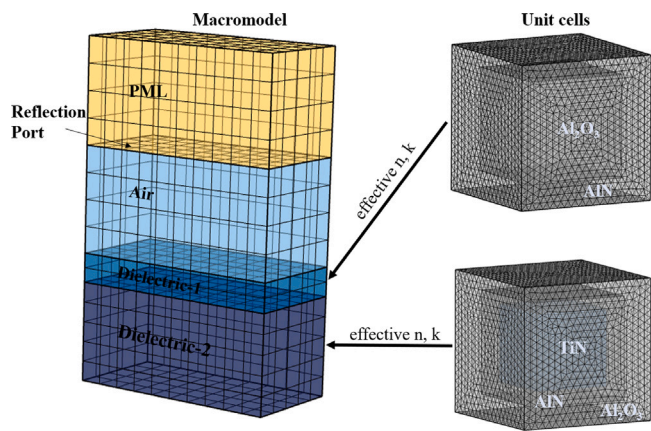
Fig. 4. Structured macro-model refined through the experimental data, with effective *n* and *k* from the unit cells, for the absorber coatings.

Fig. 6. Graph showing the comparison between the agglomerates achieved after using different methods.
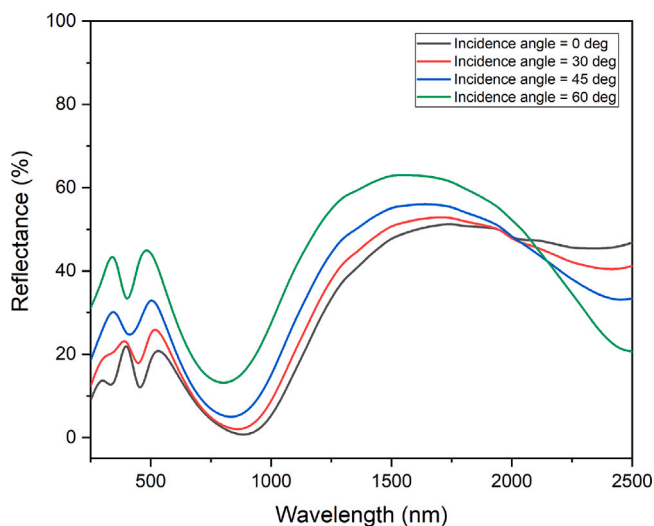

Fig. 5. Results from numerical simulations of a macro-model: Reflectance curve at normal incidence, of the prepared macro-model.

Dielectric-2 received its *n* and *k* values from a unit cell that consists of a matrix of alumina with 22% of AlN and 16% of TiN inclusions inside a AlN matrix. Fig. 5 shows the computed reflectance spectrum from the macro-model at different angles of incidence, refined with experimentally determined parameters. This presents low reflectance (high absorbance) in the visible band and high reflectance (less absorbance) in the IR region, as envisaged. It is clear from Fig. 5 that, at 60° angle of incidence, the composite gains about 20% more reflectance in the visible spectrum and loses about the same in the IR spectrum, compared to 0° angle of incidence. An important feature to note here is the same trend of reflectance for all angle of incidence in the entire spectrum. This signifies that the optical performance of the composite does not change much at the grazing incidence.

Another important point to note in Figs. 1 and 4 is the different shape of inclusions in the unit cell. The shape effect of the inclusion is insignificant in the simulations, as the wavelength range of interest is much larger than the size of the inclusions.

3. Synthesis of AlN − TiN dielectric composite

Several layers of TiN NPs embedded in a AlN matrix were synthesized, one on top of the other, making it a single composite of a thickness of few hundred nanometres. Each single layer of TiN NPs
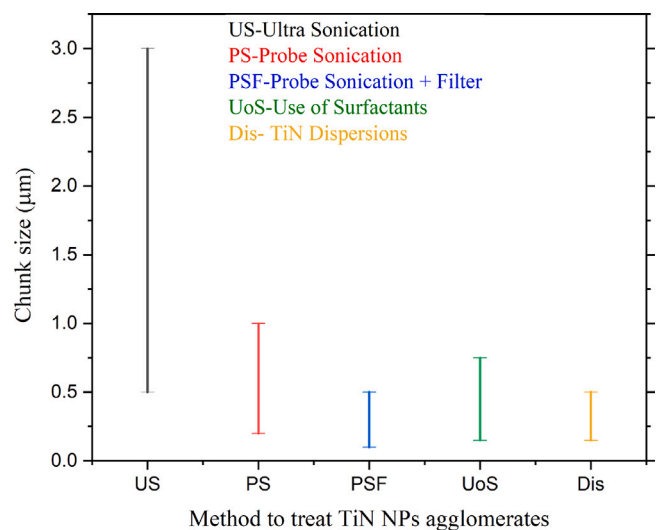
embedded in a AlN matrix was obtained first by dispersing TiN NPs onto the previous layer from a liquid suspension. A conformal film of AlN is then deposited on to the TiN dispersion. Two approaches were adopted to obtain the TiN NPs suspension: the first starting from dry powders of TiN (nominal diameter 20 nm, Goodfellow) followed by suspension in deionized water; the second by directly adopting a ready-made suspension (nominal diameter 20 nm, US Research Nanomaterials Inc.). In Section 4 we will analyse the two kind of composites, one where TiN NPs dispersion comes from the preparation based on dry powder and the other where the dispersion comes from the ready-made suspension. This will be accomplished by making a clear comparison with the differences in the SEM images, XPS analysis, electrical conductivity measurement and optical measurements.

3.1. TiN *nanoparticles suspension from dry powder*

The preparation made from TiN dry powder (approx. 20 nm particle diameter, purchased from Goodfellow Suppliers) and water showed the presence of several large chunks of aggregated nanoparticles. This became evident when bigger clusters precipitated at the bottom of the beaker, if the solution was kept stationary for several hours. SEM and scanning transmission electron microscopy (STEM) analysis confirmed the spherical shape and the diameter of 15–25 nm of the TiN components, as well as their agglomeration in chunks of few micrometres size. Clearly, for achieving good optical properties, it is crucial to have the TiN NPs in a well-dispersed state and several methods were adopted to disaggregate the chunks of TiN NPs.

A bath ultrasonic cleaner (VWR, 45 kHz, 80 W) was used first. After subjecting the TiN NPs solution to sonication for hours, no there were no noticeable differences in the size of NP agglomerates. Secondly, a probe sonicator (Q500, 20 kHz, 500 W) was employed, as the direct contact with the solution was expected to result in a better action onto the aggregates. The use of a probe with suitable size can greatly reduce the processing time and ensure the entire volume of the solution is processed properly. The volume of the solution is directly linked to the probe diameter, which meant that, for sonicating small volumes of liquid (20–250 ml), a probe with 12.7 mm diameter ideal for such volume, was used. It is clear, from the graph in Fig. 6, that probe sonication greatly reduced the size of the agglomerates, resulting in the range 100–500 nm with very few chunks close to 1 μm.

With the objective of further reducing the size of TiN agglomerates, the probe sonicated solution was filtered, using a paper of pore size
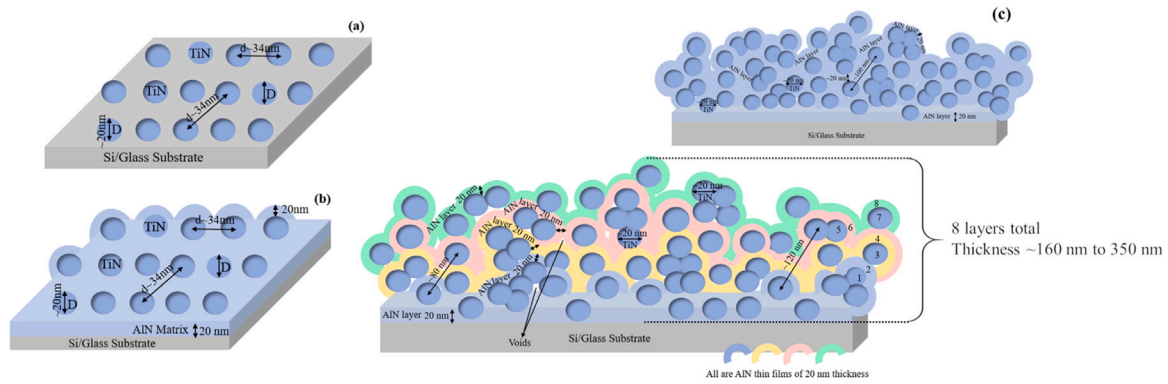
Fig. 7. Schematic of the steps included in the synthesis of a composite; (a) Step 1: Distribution of TiN NPs on Si/Glass substrate. (b): Step 2: Covering TiN NPs with a thin film of AlN. (c) Step 3: Repeating Steps 1 and 2 several times to get a composite of the desired thickness.
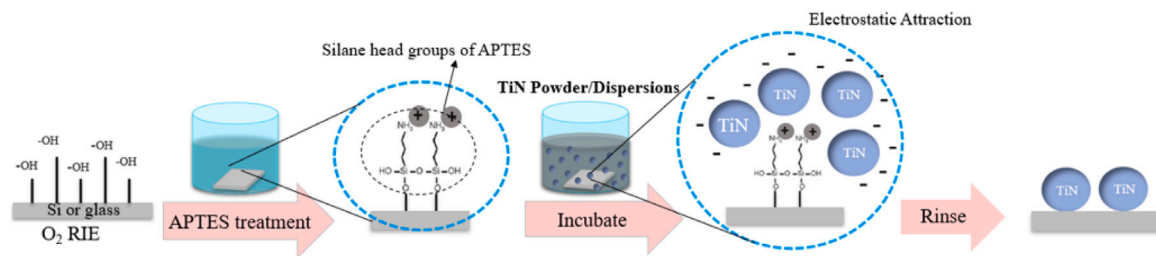

Fig. 8. Detailed experimental process for the preparation of the composite: Distribution of TiN NPs over Si/glass substrate.
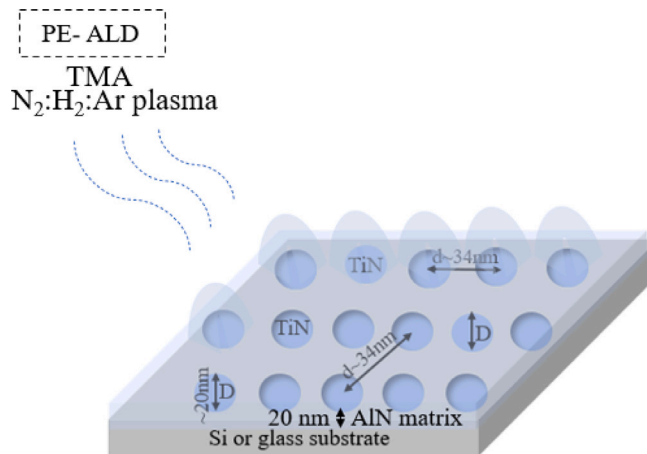

Fig. 9. Detailed experimental process for the preparation of the composite: AlN thin film over TiN NPs laid on Si/glass substrate.

Fig. 10. SEM images showing approximately 20% volume fraction of distributed TiN NPs over the substrate: 19.96% distribution of TiN NPs powder solution over Si substrate.

0.4 µm. This reduced the size of the TiN chunks to nearly 200 nm. For better dispersibility of TiN NPs solution, chemical functionalization was carried out by adding surfactants. In the literature, we could not find any conclusive work specifically dealing with TiN NPs. In addition, it has been observed that none of the common surfactants (e.g. Ficoll 400, Tween 80, Chitosan and PEG-400), is able to stabilize the TiN dispersions [35]. We chose, $Polyvinylpyrrolidone - - - PVP$ and $Polyethyleneimine - - - PEI$ as stabilizers that are well suited for particles that have a metallic behaviour, but neither worked well for the stabilization of the TiN dispersions. Fig. 6 summarizes the results of the various strategies adopted in order to disaggregate/remove TiN NPs aggregates into the solution obtained from dry powders. For comparison, it also includes the ready-made solution by US Research Nanomaterials Inc.
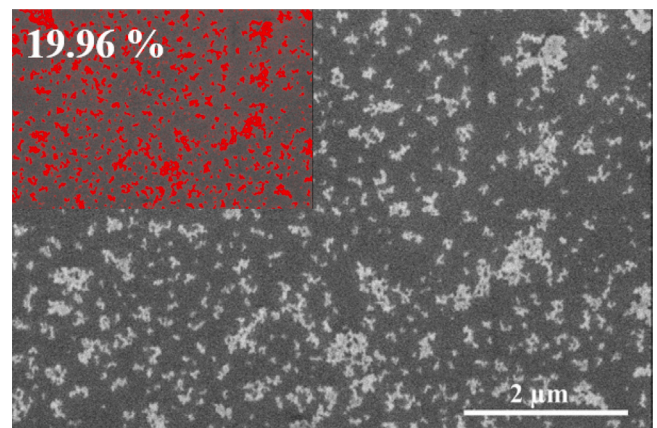
3.2. TiN Nanoparticles dispersion onto underlying surfaces

TiN NPs from liquid solution (either obtained from dry powder or ready-made one) were laid on an Si wafer by wet incubation method. They were then conformally coated with thin film of AlN, via plasma-enhanced atomic layer deposition PE-ALD [36–38], as shown in Fig. 7. The steps (a) and (b) of Fig. 7 were repeated several times, to obtain a composite with thickness of several hundred of nanometres, as illustrated in step (c) of Fig. 7.

Among wet-chemistry synthesis routes for nanostructure fabrication [39], incubation proves to be a simple, cost-effective process, with rather easy control over the distribution of particles. In this process, the Si substrate is submerged into the nanoparticles solution and incubated for a controlled time, during which nanoparticles progressively undergo physisorption adhesion onto substrate surface. Parameters like solvent,
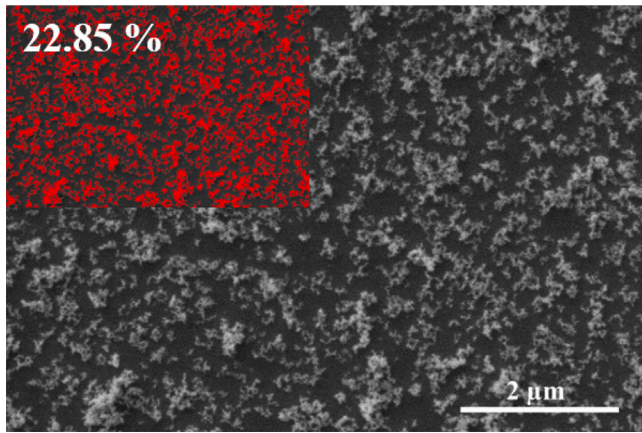
Fig. 11. SEM images showing approximately 20% volume fraction of distributed TiN NPs over the substrate: 22.85% distribution of TiN dispersions over Si substrate.
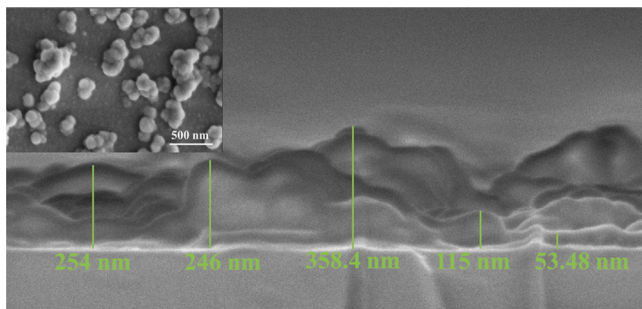

Fig. 12. Cross-section SEM images of the prepared composites: Composite-1 prepared with TiN powder.
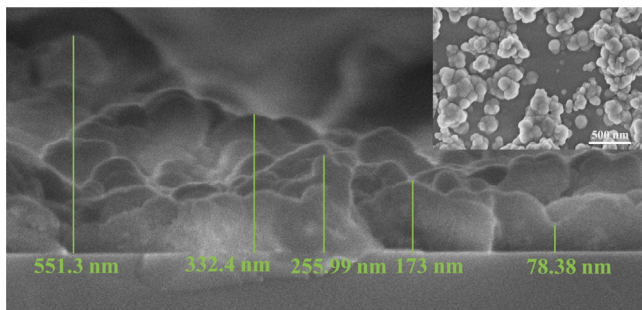

Fig. 13. Cross-section SEM images of the prepared composites: Composite-2 prepared with TiN dispersions.

particle concentrations, type of nanoparticles to be deposited and time of incubation, play an important role in nanoparticles deposition. All these parameters were fine-tuned in several experiments to obtain the desired distribution of TiN NPs. To improve the interaction of TiN NPs with the underlying surface (i.e. Si wafer at the beginning, AlN conformal layers by PE-ALD for the subsequent steps), a method called surface functionalization was adopted [40], in which we functionalized the underlying surface with APTES ((3 − Aminopropyl)triethoxysilane) ((99%) Sigma Aldrich). APTES activates the Si surface by creating stable amino-terminations suitable for nanoparticle capture. The presence of hydroxyl groups on the surface is an essential requirement for the process of silanization [41–43]. Silanization refers to the process of functionalizing the surface with silane solution that results in the formation of a silane monolayer. For this purpose, the surfaces receiving TiN NPs were functionalized where they were treated using

oxygen plasma by a reactive ion etching equipment (*Plasmatherm* 790 *RIE*) for 3 min. Oxygen plasma promotes −OH groups on the surface of the substrate, which covalently bind with the positively charged silane head groups from APTES. At the end of plasma treatment, the substrates are immediately submerged in an air-tight glass container with 20 mM solution of APTES in ethanol, for 2 h. Substrates are successively taken from the APTES solution, washed with ethanol so that the loosely attached silanes are removed and dried under nitrogen flux. The substrates are then dipped in the solution of TiN NPs (concentration 0.5 mg/ml) for 3 h. In this step, the negatively charged TiN NPs stick to the positively charged Silane head groups of APTES on the surface. Finally, the substrates are washed thoroughly with water, for the removal of loosely or unbound TiN NPs, and dried with nitrogen. A detailed experimental process for the distribution of TiN NPs on the Si and glass substrate is described in Fig. 8.

3.3. AlN *Conformal coating by (PE-ALD)*

The AlN layer over the distribution of TiN NPs, was grown by the PE-ALD reactor (Beneq TFS 200). Precursor Trimethylaluminium $Al_2(CH_3)_6$ (TMA) and a proper mixture of N_2:H_2:Ar gases with a flow ratio of 100/80/30 ppm, were used (ALPHAGAZ, $\geq$ 99.9999% − mol less than 0.5 ppm of H_2O mol impurity) [44]. The AlN films were grown by employing a sequence of four steps: TMA (0.1 s), N_2 purge (5 s), N_2:H_2:Ar plasma (20 s), and N_2 purge (5 s). The deposition temperature was set to 250 °C. The plasma power was set at 100 W. The above sequence was repeated through 275 *cycles*, to deposit a AlN layer of about 20 nm thickness. The process, of using a thin film of AlN to cover the TiN NPs laid over the substrate, by PE-ALD, is illustrated in Fig. 9.

For the second distribution of TiN nanoparticles onto the AlN film, which constitutes the 3rd layer of the composite, the process was repeated for silanization, but now the AlN layers were functionalized with 20 mM solution of APTES with toluene as solvent [45]. This second distribution of TiN nanoparticles was again coated with 20 nm of AlN, which constitutes the fourth layer in the composite. A total of eight layers were created to prepare the composite of the desired thickness, starting with the distribution of TiN NPs (1st layer) and ending with the AlN film (8th layer), distinctly seen in Fig. 7(c).

4. Results and discussion

4.1. SEM analysis of the AlN − TiN composite dielectric

To estimate the volume fraction of TiN NPs, we considered the area covered by in-plane SEM images, in sub-monolayer deposition conditions. We assumed that the fraction of area covered by TiN NPs corresponds to the volume fraction in the AlN matrix. For this purpose, SEM images were analysed by *ImageJ* software. Figs. 10 and 11 show nearly 20% surface coverage fraction of TiN NPs distributed over the Si substrate (indicated by red the zone, with colour threshold for area calculation). Despite the manual approach, this result is well in line with the targeted value. The comparison of the volume fraction with the area coverage is good as, according to the calculations, the volume fraction is 0.94 times the area coverage. Assuming the configuration where the surface coverage is the projection on the surface, we can write $V_c = S_c (4/3)(r/a)$, where V_c is the volume coverage of TiN NPs on the substrate, S_c is the surface coverage (projection) of the TiN NPs over the substrate, r is the radius of the TiN NP and a is the side of the single unit cell.

Figs. 12, 13 show the cross-section, as well as the top view, of the final composites, at the end of the layering process, which includes four distributions of TiN nanoparticles and four AlN films depositions by ALD alternating each other. Images clearly show that TiN NPs were conformally coated with AlN. Repeated layers of TiN NPs distribution and AlN thin film leads to a high surface roughness of the final composite. Cross sectional views reveal non-constant thickness, ranging from 150 nm to 560 nm, because of the piling-up of TiN NPs in the various positions of the substrate at the end of the production process.

4.2. XPS analysis of the AlN − TiN composite dielectric

To verify the elemental composition of our samples, particularly in respect to the presence of contaminants and to the in-depth distribution of the main constituents (namely Al, N and Ti), XPS was carried out with a *Kratos Axis Ultra DLD* instrument using Al (1486.6 eV) X-ray source at normal incidence angle with respect to the surface and a argon ion gun (4 keV) for etching.

Fig. 14(a) shows the results of the XPS survey scans for both types of composite before the Ar+ etching. Aluminium and nitrogen are dominant at the surface, as expected. Prominent oxygen peaks indicate that the surfaces of the topmost AlN layer of both composites is strongly oxidized. In fact, the surface of AlN films is prone to oxidation, and the emergence of different forms of oxides and hydroxides, on its surface, has been reported [46–49]. In addition, carbon, fluorine and chlorine are also observed and assigned to surface contaminations, the last two with intensities close to instrument sensitivity limit.

Fig. 14(b), (c) shows the elemental composition profile of the two composites over a total etching time of 15 min. The Si signal and the oxygen linked to Si, appearing and becoming dominant at larger etching times, has not been considered in the calculation of the percentages, aiming at emphasizing the trends of the element of interest. With respect to surface composition, three main differences in both composites are highlighted by in-depth profiles.

Firstly, the carbon intensity drops to a very low value, indicating the substantial absence of carbon impurities inside the composites. This in turn suggests that, despite the low temperature of deposition, there was no noticeable fusion of carbon containing ligands from TMA and the precursors used were completely decomposed [50]. In fact, if methyl groups from the Al precursors were trapped in the film, this would have given rise to a substantial amount of carbon. In summary, the absence of a carbon signal signifies that neither the deposition of TiN NPs (four repetitions in both composites) nor the deposition of AlN thin films (four repetitions in both composites) introduced carbon impurities.

Secondly, the amount of oxygen shows a significant drop after the first steps of etching in both composites, suggesting that a considerable portion of it was the result of atmospheric oxidation. Yet, after the initial drop, the two curves show an increase up to remarkable level of oxygen, which remains rather constant throughout the composites volume. This is ascribable to oxidation taking place during composites preparation steps, where samples are exposed to the air after each AlN thin film deposition as well as to post-deposition oxygen plasma treatment of AlN, the last aiming to promote TiN nanoparticles adhesion as explained in the previous Section 3. It can also be ascribable to oxygen contaminations affecting the deposition process of AlN itself. Aiming to investigate this last point, AlN films having thickness around 400 nm were deposited and subjected to XPS in-depth profile analysis. An amount of approximately 15% at. of oxygen was observed in the volume. This suggests the presence of oxygen contamination sources (e.g. moisture) in the reactor chamber and/or in the precursor or gas lines and, consequently, the presence of Al_2O_3 or aluminium oxynitride (AlON) within the AlN film. Favourably, AlN, Al_2O_3 and AlON, all three are optically transparent materials in the near-ultraviolet, visible, and midwave-infrared regions of the electromagnetic spectrum, which would not have a major impact on the optical properties of the composites.

The third difference in the depth profile with respect to surface composition is the appearance of a titanium signal after a certain etching time. This grows until a fairly constant value is attained throughout the composite volume. This is clearly related to the presence of TiN NPs, which are completely embedded inside the AlN matrix, as expected.

It is worth notice that, because the X-ray spot dimension (700×300) μm is much larger than the dimension of TiN nanoparticles and the spacing between them, the profiles represent the average composition over the spot size. Moreover, due to the high roughness of both samples, resulting from random distribution as well as agglomeration

of TiN nanoparticles (as unveiled by SEM cross-sections in Figs. 12, 13, composition averaging should be considered also in the vertical direction. In this respect, the etching of the thinnest regions, where no TiN particles are present, quickly reaches the Si substrate, introducing an oxygen contribution related to SiO_2 on the substrate surface. On the other hand, the appearance of the Ti signal only after a certain etching time confirms that the TiN particles are all completely covered by AlN, in the area averaged by the XPS beam spot.

To further investigate the chemical state and the nature of bonding of aluminium, nitrogen and oxygen, high resolution XPS scans were acquired for Ti2p, O1s, Al2p and N1s orbitals, for both prepared composites, as shown in Fig. 15. The high-resolution scans are collected after an etching time of 900 s, so that the information provided is ascribable to the volume fraction in the bulk of the composite.

The complex combination of peaks and satellite features of Ti2p peak, as shown in Fig. 15(a), is ascribable to TiN, TiO_2 and TiO_xN_y [51, 52]. The high resolution scan of Ti2pfor composite dielectric 2 shows the analysis with fitting of the background, TiN, TiO_xN_y, TiO_2 along with a perfect fitting of the experimental data. Similar general features were obtained for the Ti2p of composite dielectric 1, which is not detailed further here. The first Ti2p3/2 peak and the third Ti2p1/2 peak at 454.7 eV and 460.6 eV respectively, are signature of TiN. The shaded yellow region in Fig. 15(a) shows the analysis for the TiN reference that was created by physical vapour deposition (PVD) in our laboratory. The binding energy of our experimental data compares well with that of the internal reference. The satellite features shown in cyan may be attributed to TiO_xN_y and TiO_2, which also supports the presence of oxygen in the composite. This could have happened due to the exposure of TiN NPs with atmospheric oxygen over a long time.

The peak of Al2p appears at 75.6 eV for both the composites. Due to the closeness of the Al2p energies from Al − O and Al − N [53,54] the observed peak cannot unambiguously be associated to one of the species. On the other hand, the presence of both oxygen and nitrogen in our composites suggests that the observed Al2p peak includes the contribution of both species. The N1s peak is observed at 397.9 eV for both composites. As with the Al2p peak, the measured binding energy value of N1s is compatible with the cases of N bonded to Al and N bonded to Ti [55], which are nevertheless both present in the composites. Moreover, aluminium oxynitride AlON shows Al2p energy of similar values preventing a clear assessment of the possible oxidized species.

A single O1s peak was observed at 532.5 eV. According to the literature, the binding energy of O1s peak for metal oxides appears at 529–530 eV [56]. This makes it clear that no TiO_2 is present. The energy of observed O1s peak matches pretty well the case of O bonded to Si [57] from the substrate. The observed energy is also very close to the energy of O linked to Al (531.1 eV) which justifies that a fraction Al_2O_3 is also present in the composites. It is also possible to have a fraction of oxygen from Ti − O − N and O − Ti − O, the energy which was observed in the high resolution scan of Ti2p. There is also a high probability that the oxygen is chemisorbed on the surface of the TiN nanoparticles, as the naked particles were in contact with the air for a long time after deposition.

From the above analysis, it is fair to say that there is a thorough consistency in the two composites, in terms of synthesis of AlN thin films by PE-ALD, from the two approaches, and chemical composition. Furthermore, no other element was detectable in the XPS scans that distinctively shows the stability of TiN and AlN. In addition, no material diffused into any other during their synthesis.

4.3. Electrical conductivity measurements

Considering the perspective application of the composite, as one of the major components in solar selective coatings, it is necessary for the composite to behave as a dielectric. To test the electrical behaviour of the composite, impedance spectroscopy measurements were carried
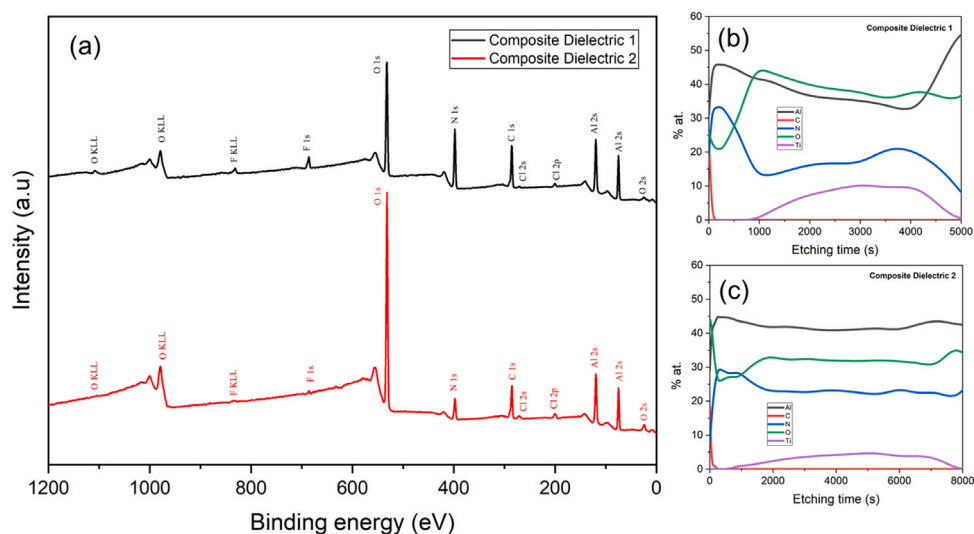
Fig. 14. XPS results of the two composite dielectrics. (a) Survey scans of composite dielectric 1 and 2. (b) Elements present during XPS scan of composite dielectric 1, until reaching the Si interface. (c) Elements present during XPS scan of composite dielectric 2, until reaching the Si interface.
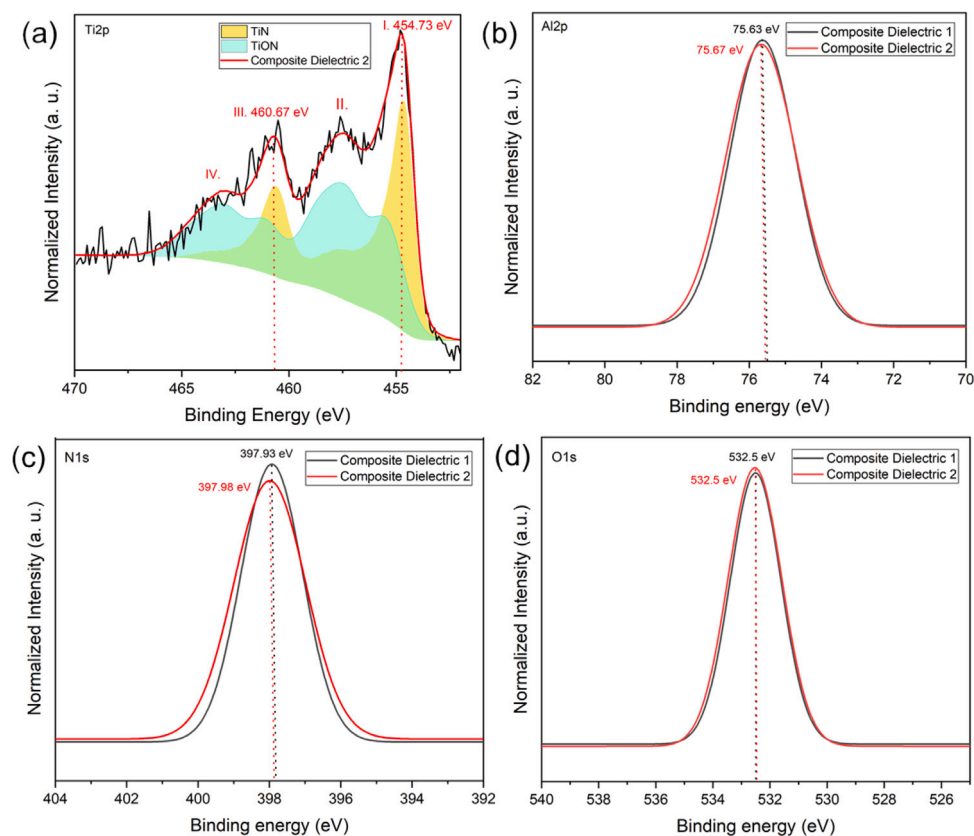

Fig. 15. The comparison of narrow scans acquired after 900 s of Ar+ sputtering, of composite-1 and composite-2: (a) Ti2p, (b) Al2p, (c) N1s, (d) O1s.

out using a Novocontrol Alpha-A Impedance Measurement System. Conductivity can be deduced from the impedance measurements for the known sample geometry. All measurements were made at room temperature.

The high roughness of the composite made it necessary to cover both sample faces with a metallic layer (Platinum, Pt) to create a constant electric potential across the surfaces. This was done by coating both sides of the sample with a 10 nm film of Pt, by sputtering technique using *Leica EM ACE 200*. It is worth noting that the deposition is done on both top and bottom surfaces of the sample, hence the silicon

substrate itself is part of the measured materials sandwich. In order to distinguish the impedance behaviour of the composite from that of the silicon substrate, a reference sample was prepared in which the Pt was deposited on the two surfaces of a silicon substrate only.

The samples were then placed between the two parallel plates of the sample holder of the spectrometer. The platinum Pt layer ensured a good electrical connection between the entire (rough) surface of the composite and the (flat) top electrode of the sample holder. Due to the non-regular thickness of the composites, the impedance results have been referred to the average thickness within the electrode area.
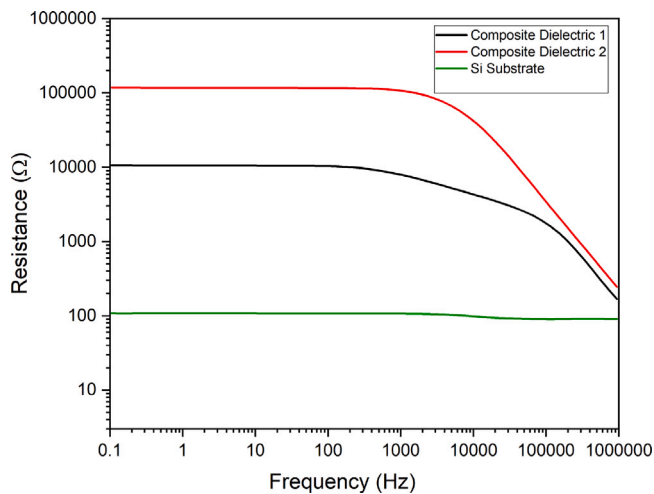
Fig. 16. Electrical conductivity measurement of dielectric composite 1, 2 and bare Si substrate.

Fig. 17. Comparison of reflectance of the two composite dielectrics and the numerical macro-model.

Fig. 16 shows the results of impedance spectroscopy measurements, in terms of impedance module $|Z|$ as function of frequency. Although bare Si has a resistive behaviour throughout the frequency range investigated, at high frequencies, the samples including the composite multilayer behave as capacitors (one order of magnitude decrease in $|Z|$) per one order of magnitude increase in frequency), as expected. At low frequencies, composite samples basically behave as resistors, as $|Z|$ does not depend on frequency. In this region, we observe a difference of about one order of magnitude in the resistive component of the composite.

However, considering both the resistive part at low frequencies and the capacitive part at high frequencies, we observe that the cut-off frequencies of the two composites $1/RC$ are separated by one order of magnitude, in good agreement with resistance difference. This suggests that the capacitive behaviour of the two composites is basically the same.

4.4. Optical characterization

The optical reflectance in the visible and IR range was measured using the *Perkin Elmer Lambda 750 Spectrophotometer*. Both deposited layers of composites 1 and 2 are shown respectively in Figs. 12 and 13. The SEM image for composite dielectric 1 shows partial coverage of the silicon substrate with agglomerates ranging from about 50 to 360 nm, while the image corresponding to that of the composite dielectric-2 shows also partial coverage, but with slightly more surface coverage, and agglomerates ranging from about 80 to 550 nm.

In the numerical simulation, shown in Fig. 4, we modelled this case by considering the XPS results; the bottom layer is made of composite $(AlN - TiN - Al_2O_3)$ of thickness 232 nm and the top layer is made of composite $AlN - Al_2O_3$ with 68 nm thickness. The silicon substrate is modelled as a perfect electric conductor (PEC) boundary condition, which totally reflects the EM waves. Fig. 17 shows the comparison between the measured and the computed reflectance at normal incidence of both composites. The dielectric curves show a difference in magnitude in the IR region. This is explained by the fact that composite-2 has more absorbing material than composite-1 and much bigger agglomerates. The simulation curve shows similar reflectance level, in the visible range, compared to the measurements, for both composites. However, for wavelengths at the IR region, the predicted reflectance shows higher values than observed. This is explained by the fact that the model surfaces are uniform, while the two samples have very rough surfaces. The important thing to note is that all curves filter behaviour at 1 μm, as predicted.
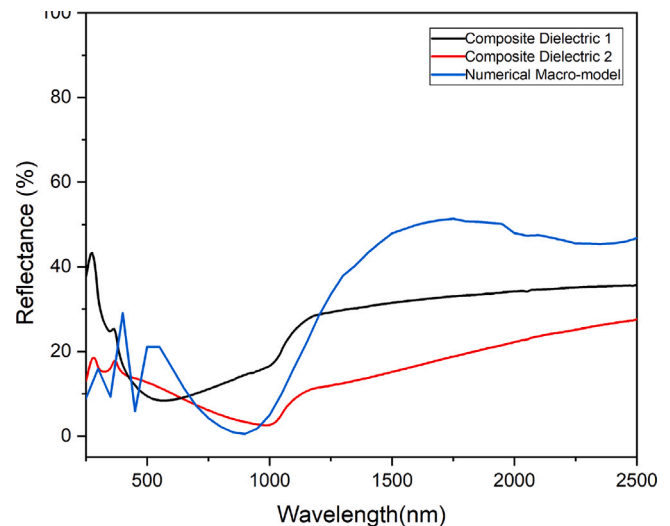
5. Conclusion

In this paper, we presented results of the production and characterization of a composite $(AlN - TiN)$ solar absorber for concentrated solar power (CSP) applications. The composite was constructed with a stack of layers, by alternating the adsorption of TiN NPs, and the deposition of a conformal AlN coating. The choice of TiN and AlN was made on the basis of their electrical and thermal properties, matching the strict requirements of high-temperature solar absorbers for CSP. The fundamental design elements, namely the size of TiN particles and their volume fraction in the AlN matrix, were defined before the experimental phase through numerical simulations. This allowed the fine-tuning of the composite structure to achieve the targeted performance.

Although affected by aggregation issues, which are particularly severe at the nanoscale dimensions of the supplied NPs, wet-chemistry methods adopted for better distribution allowed a reasonably good control of the uniformity and the volume fraction of the TiN component of the composite dielectric film. The PE-ALD adopted for embedding TiN nanoparticles into the AlN matrix, was shown to be a good approach to address this task, thanks to the high conformity of the PE-ALD coating, which allowed the complete burying of TiN nanoparticles, even in the case of aggregates.

The overall characterization results collected from the two composite samples confirmed the design of a structure that was in agreement with that modelled computationally. In particular, the optical characterization, where the reflectance in the visible region was shown to be close, for the two composite dielectrics and the numerical macro-model. In all the three cases, a well-defined filter is also observed at 1 μm, as anticipated.

The composite described in this article represents a fundamental element of a more complex structure, the emergence of metamaterials. Producing an ideal metamaterial based selective absorber structure by placing an array of resonators on top of these composite dielectrics, will create potential opportunities, especially in the field of solar energy harvesting.

Declaration of competing interest

The authors declare that they have no known competing financial interests or personal relationships that could have appeared to influence the work reported in this paper.

Acknowledgements

References

[1] J. Sladek, V. Sladek, M. Repka, S. Schmauder, Mixed FEM for quantum nanostructured solar cells, Compos. Struct. 229 (2019) 111460, http://dx.doi.org/10.1016/j.compstruct.2019.111460, URL https://www.sciencedirect.com/science/article/pii/S0263822319323864.

[2] M. Paggi, M. Corrado, M.A. Rodriguez, A multi-physics and multi-scale numerical approach to microcracking and power-loss in photovoltaic modules, Compos. Struct. 95 (2013) 630–638, http://dx.doi.org/10.1016/j.compstruct.2012.08.014, URL https://www.sciencedirect.com/science/article/pii/S0263822312003807.

[3] J.W. Lim, D. Lee, M. Kim, J. Choe, S. Nam, D.G. Lee, Composite structures for proton exchange membrane fuel cells (PEMFC) and energy storage systems (ESS): Review, Compos. Struct. 134 (2015) 927–949, http://dx.doi.org/10.1016/j.compstruct.2015.08.121, URL https://www.sciencedirect.com/science/article/pii/S026382231500817X.

[4] A.D.B. Ferreira, P.R. Nóvoa, A.T. Marques, Multifunctional material systems: A state-of-the-art review, Compos. Struct. 151 (2016) 3–35, http://dx.doi.org/10.1016/j.compstruct.2016.01.028, Smart composites and composite structures In honour of the 70th anniversary of Professor Carlos Alberto Mota Soares URL https://www.sciencedirect.com/science/article/pii/S0263822316000416.

[5] F. Cao, K. McEnaney, G. Chen, Z. Ren, A review of cermet-based spectrally selective solar absorbers, Energy Environ. Sci. 7 (5) (2014) 1615–1627.

[6] N. Selvakumar, H.C. Barshilia, Review of physical vapor deposited (PVD) spectrally selective coatings for mid-and high-temperature solar thermal applications, Sol. Energy Mater. Sol. Cells 98 (2012) 1–23.

[7] L.A. Weinstein, J. Loomis, B. Bhatia, D.M. Bierman, E.N. Wang, G. Chen, Concentrating solar power, Chem. Rev. 115 (23) (2015) 12797–12838.

[8] D. Kraemer, B. Poudel, H.-P. Feng, J.C. Caylor, B. Yu, X. Yan, Y. Ma, X. Wang, D. Wang, A. Muto, et al., High-performance flat-panel solar thermoelectric generators with high thermal concentration, Nature Mater. 10 (7) (2011) 532–538.

[9] D.M. Bierman, A. Lenert, W.R. Chan, B. Bhatia, I. Celanović, M. Soljačić, E.N. Wang, Enhanced photovoltaic energy conversion using thermally based spectral shaping, Nat. Energy 1 (6) (2016) 1–7.

[10] E. Commission, Clean Energy-Transition Technologies and Innovations Report (CETTIR), techreport SWD(2020), Commission to the European Parliament and the Council, 2020, URL https://eur-lex.europa.eu/legal-content/EN/TXT/HTML/?uri=CELEX:52020SC0953&rid=1.

[11] E. Randich, D.D. Allred, Chemically vapor-deposited ZrB2 as a selective solar absorber, Thin Solid Films 83 (4) (1981) 393–398.

[12] B.O. Seraphin, Chemical vapor deposition of thin semiconductor films for solar energy conversion, Thin Solid Films 39 (1976) 87–94.

[13] R.N. Schmidt, K.C. Park, R.H. Torberg, J.E. Jensen, High temperature solar coatings, in: Part I, AST-TDR-63-579, Honeywell Corporation, Hopkins, MN, 1963.

[14] G. Vijaya, M.M. Singh, M.R. Srinivas, B.S. Satyanarayana, R.S. Kulkarni, Optimization of thin film multilayered coating for absorption of solar radiation, Int. J. Chemtech Res. 7 (2015) 1045–1052.

[15] S. Zhao, Spectrally selective solar absorbing coatings prepared by dc magnetron sputtering, (Ph.D. thesis), Acta Universitatis Upsaliensis, 2007.

[16] G. Niklasson, C. Granqvist, Selectively solar-absorbing surface coatings: optical properties and degradation, in: Materials Science for Solar Energy Conversion Systems, Elsevier, 1991, pp. 70–105, http://dx.doi.org/10.1016/b978-0-08-040937-5.50008-5.

[17] U. Guler, A. Boltasseva, V.M. Shalaev, Refractory plasmonics, Science 344 (6181) (2014) 263–264.

[18] U. Guler, A.V. Kildishev, A. Boltasseva, V.M. Shalaev, Plasmonics on the slope of enlightenment: the role of transition metal nitrides, Faraday Discuss. 178 (2015) 71–86.

[19] U. Guler, V.M. Shalaev, A. Boltasseva, Nanoparticle plasmonics: going practical with transition metal nitrides, Mater. Today 18 (4) (2015) 227–237.

[20] W. Li, U. Guler, N. Kinsey, G.V. Naik, A. Boltasseva, J. Guan, V.M. Shalaev, A.V. Kildishev, Refractory plasmonics with titanium nitride: broadband metamaterial absorber, Adv. Mater. 26 (47) (2014) 7959–7965.

[21] G.V. Naik, J. Kim, A. Boltasseva, Oxides and nitrides as alternative plasmonic materials in the optical range [invited], Opt. Mater. Express 1 (6) (2011) 1090, http://dx.doi.org/10.1364/ome.1.001090.

[22] P. Motamedi, K. Cadien, Structural and optical characterization of low-temperature ALD crystalline AlN, J. Cryst. Growth 421 (2015) 45–52.

[23] H. Jensen, G. Pedersen, G. Sørensen, et al., Effect of reactive gas mass flow on the composition and structure of AlN films deposited by reactive sputtering, Thin Solid Films 230 (2) (1993) 121–127.

[24] S. Goerke, M. Ziegler, A. Ihring, J. Dellith, A. Undisz, M. Diegel, S. Anders, U. Huebner, M. Rettenmayr, H.-G. Meyer, Atomic layer deposition of AlN for thin membranes using trimethylaluminum and H2/N2 plasma, Appl. Surf. Sci. 338 (2015) 35–41.

[25] C.-Y. Lin, F.-H. Lu, Oxidation behavior of AlN films at high temperature under controlled atmosphere, J. Eur. Ceramic Soc. 28 (3) (2008) 691–698.

[26] F. Wang, R. Zhang, X. Xiu, D. Lu, S. Gu, B. Shen, Y. Shi, Y. Zheng, Study of dry oxidation of aluminum nitride on Si (111) substrate grown by metalorganic chemical vapor deposition, Surf. Rev. Lett. 10 (04) (2003) 625–628.

[27] J. Wen, J. Zhang, Y. Gao, A coupling finite element model for analysis the nonlinear dynamic magnetoelectric response of tri-layer laminate composites, Compos. Struct. 166 (2017) 163–176, http://dx.doi.org/10.1016/j.compstruct.2017.01.056, URL https://www.sciencedirect.com/science/article/pii/S0263822316321444.

[28] X. Ma, F. Wang, Z. Wei, D. Wang, B. Xu, Transient response predication of nickel coated carbon fiber composite subjected to high altitude electromagnetic pulse, Compos. Struct. 226 (2019) 111307, http://dx.doi.org/10.1016/j.compstruct.2019.111307, URL https://www.sciencedirect.com/science/article/pii/S0263822319322342.

[29] L.E.R. Petersson, J.-M. Jin, Analysis of periodic structures via a time-domain finite-element formulation with a Floquet ABC, IEEE Trans. Antennas and Propagation 54 (3) (2006) 933–944.

[30] S. Samukham, C. Vyasarayani, G. Raju, Implicit floquet analysis for parametric instabilities in a variable angle tow composite panel, Compos. Struct. 233 (2020) 111637, http://dx.doi.org/10.1016/j.compstruct.2019.111637, URL https://www.sciencedirect.com/science/article/pii/S0263822319329812.

[31] D.R.H. Craig F. Bohren, Absorption and scattering by an arbitrary particle, in: Absorption and Scattering of Light By Small Particles, John Wiley & Sons, Ltd, 1998, pp. 57–81, http://dx.doi.org/10.1002/9783527618156.ch3, arXiv:https://onlinelibrary.wiley.com/doi/pdf/10.1002/9783527618156.ch3.

[32] D.R.H. Craig F. Bohren, Absorption and scattering by a sphere, in: Absorption and Scattering of Light By Small Particles, John Wiley & Sons, Ltd, 1998, pp. 82–129, http://dx.doi.org/10.1002/9783527618156.ch4, arXiv:https://onlinelibrary.wiley.com/doi/pdf/10.1002/9783527618156.ch4.

[33] X. Chen, T.M. Grzegorczyk, B.-I. Wu, J. Pacheco, J.A. Kong, Robust method to retrieve the constitutive effective parameters of metamaterials, Phys. Rev. E 70 (1) (2004) 016608, http://dx.doi.org/10.1103/physreve.70.016608.

[34] D.R. Smith, D.C. Vier, T. Koschny, C.M. Soukoulis, Electromagnetic parameter retrieval from inhomogeneous metamaterials, Phys. Rev. E 71 (3) (2005) 036617, http://dx.doi.org/10.1103/physreve.71.036617.

[35] M. Gozin, Development of Modified Titanium Nitride Nanoparticles asPotential Contrast Material for Photoacoustic Imaging, Tech. rep, Tel Aviv University, 2014.

[36] M. Bosund, T. Sajavaara, M. Laitinen, T. Huhtio, M. Putkonen, V.-M. Airaksinen, H. Lipsanen, Properties of AlN grown by plasma enhanced atomic layer deposition, Appl. Surf. Sci. 257 (17) (2011) 7827–7830.

[37] X. Liu, S. Ramanathan, E. Lee, T.E. Seidel, Atomic layer deposition of aluminum nitride thin films from trimethyl aluminum (TMA) and ammonia, MRS Online Proc. Library (OPL) 811 (2004).

[38] V. Miikkulainen, M. Leskelä, M. Ritala, R.L. Puurunen, Crystallinity of inorganic films grown by atomic layer deposition: Overview and general trends, J. Appl. Phys. 113 (2) (2013) 2.

[39] S.C. Tjong, H. Chen, Nanocrystalline materials and coatings, Mater. Sci. Eng. R. Rep. 45 (1–2) (2004) 1–88.

[40] A. Taglietti, C.R. Arciola, A. D'Agostino, G. Dacarro, L. Montanaro, D. Campoccia, L. Cucca, M. Vercellino, A. Poggi, P. Pallavicini, et al., Antibiofilm activity of a monolayer of silver nanoparticles anchored to an amino-silanized glass surface, Biomaterials 35 (6) (2014) 1779–1788.

[41] J. Sagiv, Organized monolayers by adsorption. 1. Formation and structure of oleophobic mixed monolayers on solid surfaces, J. Am. Chem. Soc. 102 (1980) 92–98.

[42] H. Mizumachi, Adhesion science and technology, in: Proceedings of the International Adhesion Symposium, Yokohama, Japan, November 6-10, 1994, Gordon and Breach Science Publishers, Amsterdam, 1997.

[43] A.N. Parikh, D.L. Allara, I.B. Azouz, F. Rondelez, An intrinsic relationship between molecular structure in self-assembled n-alkylsiloxane monolayers and deposition temperature, J. Phys. Chem. 98 (31) (1994) 7577–7590.

[44] T. Nguyen, N. Adjeroud, S. Glinsek, Y. Fleming, J. Guillot, P. Grysan, J. Polesel-Maris, A film-texture driven piezoelectricity of AlN thin films grown at low temperatures by plasma-enhanced atomic layer deposition, APL Mater. 8 (7) (2020) 071101.

[45] B. Baur, G. Steinhoff, J. Hernando, O. Purrucker, M. Tanaka, B. Nickel, M. Stutzmann, M. Eickhoff, Chemical functionalization of GaN and AlN surfaces, Appl. Phys. Lett. 87 (26) (2005) 263901.

[46] H.M. Liao, R.N.S. Sodhi, T.W. Coyle, Surface composition of AlN powders studied by x-ray photoelectron spectroscopy and bremsstrahlung-excited auger electron spectroscopy, J. Vacuum Sci. Technol. A: Vacuum Surfaces Films 11 (5) (1993) 2681–2686.

[47] M. García-Méndez, S. Morales-Rodríguez, S. Shaji, B. Krishnan, P. Bartolo-Pérez, Structural properties of AlN films with oxygen content deposited by reactive magnetron sputtering: XRD and XPS characterization, Surf. Rev. Lett. 18 (01n02) (2011) 23–31.

[48] F. Jose, R. Ramaseshan, S. Dash, S. Bera, A.K. Tyagi, B. Raj, Response of magnetron sputtered AlN films to controlled atmosphere annealing, J. Phys. D: Appl. Phys. 43 (7) (2010) 075304.

[49] Y. Zhang, Characterization of as-received hydrophobic treated AlN powder using XPS, J. Mater. Sci. Lett. 21 (20) (2002) 1603–1605.

[50] P. Motamedi, K. Cadien, XPS Analysis of AlN thin films deposited by plasma enhanced atomic layer deposition, Appl. Surf. Sci. 315 (2014) 104–109.

[51] E.N. Kabachkov, E.N. Kurkin, N.N. Vershinin, I.L. Balikhin, V.I. Berestenko, A. Michtchenko, Y.M. Shulga, Pt supported on plasma-chemical titanium nitride for efficient room-temperature CO oxidation, 2019, arXiv preprint arXiv:1911.07321.

[52] J.B. Yoo, H.J. Yoo, H.J. Jung, H.S. Kim, S. Bang, J. Choi, H. Suh, J.-H. Lee, J.-G. Kim, N.H. Hur, Titanium oxynitride microspheres with the rock-salt structure for use as visible-light photocatalysts, J. Mater. Chem. A 4 (3) (2016) 869–876.

[53] M. Alevli, C. Ozgit, I. Donmez, N. Biyikli, Structural properties of AlN films deposited by plasma-enhanced atomic layer deposition at different growth temperatures, Phys. Status Solidi (A) 209 (2) (2012) 266–271.

[54] O.H. Kim, D. Kim, T.J. Anderson, Atomic layer deposition of GaN using GaCl3 and NH3, J. Vac. Sci. Technol. 27 (2009) 923–928.

[55] T.F.S. Inc, https://www.jp.xpssimplified.com/elements/nitrogen.php.

[56] G.R. Rao, D.D. Sarma, Systematics in the o 1s core-level spectra in transition metal oxides, LaMO 3 (M=V, Cr, Mn, Fe, Co AND Ni), Modern Phys. Lett. B 4 (04) (1990) 277–282.

[57] A.U. Alam, M.M.R. Howlader, M.J. Deen, Oxygen plasma and humidity dependent surface analysis of silicon, silicon dioxide and glass for direct wafer bonding, ECS J. Solid State Sci. Technol. 2 (12) (2013) P515.